



# Tuning higher order electric field resonances in plasmonic hexagonal arrays by oxygen-plasma treatment

Nonthanan Sitpathom<sup>1</sup> · Judith M. Dawes<sup>2</sup> · Tanakorn Osotchan<sup>1</sup> · Pisisit Kumnorkaew<sup>3</sup> · Sujin Suwanna<sup>1</sup> · Asawin Sinsarp<sup>1</sup> · Tanyakorn Muangnapoh<sup>3</sup>

Received: 23 July 2020 / Accepted: 10 April 2021 / Published online: 26 April 2021  
© The Author(s), under exclusive licence to Springer-Verlag GmbH Germany, part of Springer Nature 2021

## Abstract

Experimental and simulation studies show that a hexagonal array of polystyrene particles on a gold substrate, capped with gold semi-shells, results in increased optical confinement of the resonance modes in comparison with those for arrays without metallic substrate or capping. Well-ordered arrays of polystyrene beads were fabricated by convective deposition, a solution-based self-assembly process. The polystyrene particles exhibited strong optical concentration, with photonic and plasmonic modes as detected in optical spectra and modelling. The resonance wavelengths of the plasmonic hexagonal array were modified by treating the hexagonal arrays with oxygen plasma at fixed power of 150 W for time periods of 0–10 min. The plasma treatment reduced the vertical height of the polystyrene particles, and the resonances were tuned and sharpened after plasma treatment. This increase is attributed to the improved uniformity of the gold semi-shell coating distributed over the polystyrene particles. Additionally, the plasma treatment increased the refractive index of the polystyrene particles due to cross-linking. Devices with these plasmonic hexagonal arrays enable enhanced light–matter interactions, with the flexibility to post-tune the resonance wavelengths.

## 1 Introduction

Light–matter interactions can be effectively enhanced by strongly localizing electromagnetic fields in various nanophotonic structures. Both individual microstructures and periodic arrays of microstructures can produce optical enhancement, whether as isolated microcavities [1–3], or as regular arrays of Si [4] or SiC [5] pillars, Si nano-cones [6], nano-disks [7, 8], nanoholes [9–11], or more generally as metamaterials [12]. Individual features can exhibit localized resonances associated with microcavities, but in periodic arrays, there are additionally propagating modes which also introduce resonances. The addition of metallic layers

to the periodic microstructures further enhances the light interaction, supporting surface plasmon polaritons bound to the metal surface and guided modes within the dielectric structures [13]. These plasmonic–photonic structures have found applications as substrates for sensing [14–16], surface-enhanced Raman spectroscopy (SERS) [17–19], and photocatalysis [20]. In addition, such structures can support directed emission [13], light trapping [21], photocurrent conversion [22], and enhanced photoluminescence [23–25].

Periodic microstructures can be constructed by top–down lithographic processes, for example holographic lithography [26], or bottom–up processes, for example self-assembly of microspheres into a regular array. A periodic microstructure created from core–shell particles exhibits more complex spectral features [27] and a monolayer array of dielectric particles coated with higher refractive index dielectric or metallic layers also exhibits greater confined light inside the layers, supporting photonic, plasmonic, and hybrid plasmonic–photonic modes [28–35]. Furthermore, to ensure strong optical confinement in the monolayer array, a gold substrate hinders leakage of radiation from the monolayer to the substrate [36, 37]. Whereas, if the substrate is a low-index dielectric, the

✉ Tanyakorn Muangnapoh  
tanyakorn.mua@nanotec.or.th

<sup>1</sup> Department of Physics, Faculty of Science, Mahidol University, Bangkok, Thailand

<sup>2</sup> Department of Physics and Astronomy, Faculty of Science and Engineering, Macquarie University, Sydney, NSW, Australia

<sup>3</sup> National Nanotechnology Center (NANOTEC), National Science and Technology Development Agency (NSTDA), Pathum Thani, Thailand

particle monolayer behaves like a free-standing array, with sharp resonance peaks in the transmission spectrum [38].

An advantage of using polystyrene beads to form nanophotonic structures is their chemical compatibility with many organic molecules, for example with conjugated polyrotaxanes [39], Rhodamine B [40], tert-butyl Rhodamine B [41], and 4-(dicyanomethylene)-2-*tert*-butyl-6-(1,1,7,7-tetramethyljulolidin-4-yl-vinyl)-4*H*-pyran (DCJTB) [42]. These doped polystyrene beads enable enhanced lasing emission in the periodic structures.

A key factor in enhancing light–matter interactions is matching the microstructure resonances to the molecule of interest or the excitation light, for example by changing the cavity size [43] or refractive index. The polystyrene particle shape and diameter can also be modified via plasma treatment using oxygen [43], argon [44], chloroform [45], or a mixture of gases [46]. During the plasma treatment, polymer chains in the polystyrene may become cross-linked [47–49], but this may be prevented by treating with a mixture of oxygen and methanol [50]. Various factors affect the resulting shape and size of the polystyrene particles, including the temperature of the plasma chamber [51], power of the plasma, and treatment time [52]. Vogel et al. showed that the particles' height and diameter decrease non-linearly with plasma power and treatment time, and the substrate material influences the treated particles' shape [43]. The particle–particle bridges affect the resulting diameter of the plasma-treated particles [52, 53]. Moreover, the refractive index of the polystyrene tends to increase after plasma treatment [54–56]. The Lorentz–Lorenz equation [57] implies that the refractive indices depend on the mass density. Plasma treatment of polystyrene tends to increase the mass density, as shown by Bilek et al. using X-ray and neutron scattering and spectral analysis [58].

In this paper, we present a geometrically modifiable plasmonic microstructure with strong near-infrared optical field confinement. By modifying the particle size and period, we tune the resonance wavelengths, and we observe propagating mode resonances comparable to those for a free-standing monolayer [38] or array of SiC pillars [5]. The hexagonal monolayer array was prepared by convective deposition of polystyrene beads on a gold substrate [59, 60]. The monolayer was then capped with an ultra-thin gold film to create the plasmonic hexagonal array. To tune the optical resonances, the hexagonal array was treated by oxygen plasma at fixed plasma power for various time periods. The morphology of the polystyrene particles with and without oxygen-plasma treatment was observed by scanning electron microscopy (SEM). Energy-dispersive X-ray spectroscopy (EDX) was used to map the gold semi-shell distribution profile, to inform modelling of the structures.

In our numerical studies, a finite-difference time-domain method was used to explore the optical resonances of the hexagonal array using MIT Electromagnetic Equation Propagation (MEEP), which is an open software package [61]. In the simulations, the electric permittivity of gold was described by the Drude–Lorentz model [62]. The dielectric constants of the non-dispersive materials, polystyrene and glass, were assumed to be constant [63, 64]. The Quality (*Q*) factors of the plasma-treated and untreated arrays were calculated to estimate the light confinement.

## 2 Materials and methods

### 2.1 Monolayer fabrication

The glass substrates were cleaned by Alconox detergent to remove contamination, and then isopropyl alcohol at 60 °C to create a hydrophilic surface. An 80 nm-thick film of gold was thermally evaporated on the substrate. Polystyrene spheres (930 nm diameter and CV < 3%, Thermo Fisher Scientific) were assembled on the gold film by convective deposition at room temperature and relative humidity around 65%. A volume of 10 µL of the polystyrene sphere suspension (10% w/v concentration) was dropped on the substrate under a cleaned glass blade, which was fixed at an angle of 45°. The glass substrate moved with a velocity of 18 µm/s relative to the fixed blade. To achieve monolayer deposition with large crystal domains, vibration assistance using a mechanical wave driver at 20 Hz was applied to the substrates during the deposition [59].

An oxygen plasma was used to change the diameter, height, and shape of the 930 nm polystyrene spheres. The oxygen gas was sparked with a high-voltage electrode inside the vacuum chamber at a pressure of  $2 \times 10^{-2}$  mbar. The sparking power was 150 W, and the treatment time was varied from 0 to 2.5 min, 5.0 min, 7.5 min, and 10 min. Finally, the treated monolayer of polystyrene particles on the gold film was capped with a 20 nm-thick gold film by thermal sputtering for 5 min.

### 2.2 Optical measurements and morphology observation

The optical absorption spectra were recorded by illuminating the samples at normal incidence with broadband white light from a halogen lamp (300 nm–1200 nm). The measured reflection spectrum was normalized to the source profile. The absorbance was calculated from the reflectance, assuming negligible transmission through the film.

The morphology of the plasmonic hexagonal arrays with and without oxygen-plasma treatment was observed by scanning electron microscopy from above and from the

side in cross-section. Additionally, to investigate the profile distribution of the gold film on the polystyrene particles, energy-dispersive X-ray spectroscopy was used with colour mapping to determine the degree of coverage of the gold.

### 2.3 Finite-difference time-domain simulations

Results of finite-difference time-domain (FDTD) simulations, in which Maxwell's equations are solved in the spatial and time-domains, were compared with the experimental results. The unit cell, consisting of a monolayer of polystyrene particles with a 80 nm-thick gold substrate, and capped by a 20 nm-gold film on top of the particles, is sketched in Fig. 1a. For results of additional simulations on different unit cell arrangements, please see the Supplementary Information. The diameter of the polystyrene particles was fixed at 930 nm and the height ( $h$ ) was varied to model the effect of the oxygen-plasma treatment. On top of the unit cell, there was a perfectly matched layer to absorb back-scattered radiation. Periodic boundary conditions were applied in the xy-plane. In all simulations, the Gaussian plane wave (central frequency of  $3.0 \times 10^{14}$  Hz and bandwidth of  $3.0 \times 10^{14}$  Hz to cover the spectral range of interest) was generated above the monolayer and propagated in the direction normal to the monolayer. The computational time-step was  $0.67 \times 10^{-2}$  fs and the grid resolution was 7 nm. The simulation was terminated when the electric field strength at the points of interest decayed by a factor of  $10^{-6}$  from the initial values.

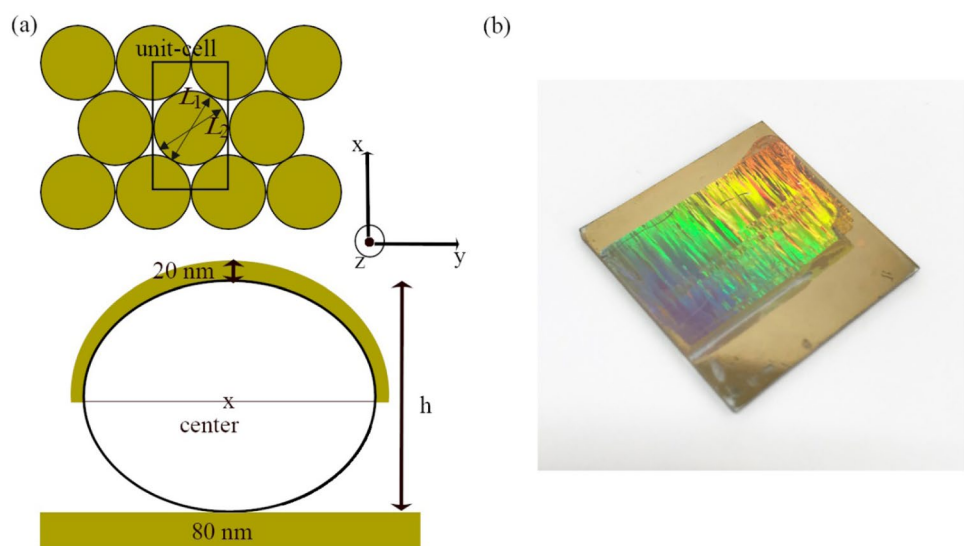
For the simulations, the refractive indices ( $n$ ) of the polystyrene and glass were assumed to be 1.58 and 1.51, estimated for wavelengths of 886 nm [63] and 872 nm [64], respectively. However, plasma treatment can increase the surface refractive index of polystyrene up to 2.1 [54].

According to our numerical investigation (explained further in the Supplementary Information and in Sect. 3.2 below), the shapes of the absorption spectra can be matched for various refractive index distributions in the polystyrene particles. For simplicity, we assumed a homogeneous refractive index for the simulations. Assuming the dimensions estimated from SEM and optical measurements, we found a homogeneous refractive index of 1.7 throughout the entire polystyrene particle gave the best agreement with the observed spectra after plasma treatment. The electric permittivity of gold was modelled using the Drude–Lorentz expression [62]:

$$\varepsilon(\omega) = \varepsilon_{\infty} - \frac{f_0 \omega_p^2}{\omega(\omega - i\Gamma_0)} + \sum_{j=1}^k \frac{f_j \omega_p^2}{(\omega_j^2 - \omega^2) + i\omega\Gamma_j}. \quad (1)$$

Here,  $\varepsilon_{\infty}$  is the electric permittivity at ultra-high frequency, approximately 1. The second term is given by the Drude model, which assumes electrons move freely. The last term is the Lorentz model describing the bounded electron motion. In Eq. (1),  $\omega_p$  is the plasma frequency for intraband transitions, and  $f_0$  and  $\Gamma_0$  are the oscillator strength and damping constant, respectively. The Drude model assuming free electrons with no restoring force does not adequately describe the gold electric permittivity in the visible light region. Under white light illumination, there are interband electron transitions causing rapid changes in electric permittivity. To capture this phenomenon, the bounded electron model (Lorentz model) with several oscillators is required. The Lorentz model incorporates  $k$  oscillators with frequency  $\omega_j$ , strength  $f_j$ , and lifetime  $1/\Gamma_j$ . The Drude–Lorentz model was used to model the properties of gold over the energy (wavelength) range of 0.2–5 eV (248–6000 nm) [62].

**Fig. 1** **a** Simulation model of the hexagonal-plasmonic monolayer showing a unit cell containing a particle at the centre and quarters of particles at four corners. **b** Cross-section of a deformed polystyrene particle on gold film, capped with a gold semi-shell. **c** White light photograph of an experimental fabricated monolayer of polystyrene particles on a gold substrate and capped with thin gold film



### 3 Results and discussion

#### 3.1 Oxygen-plasma treatment on gold-coated polystyrene particle arrays

The arrays of polystyrene microspheres (diameter of 930 nm) deposited on the gold films were treated by oxygen plasma with durations of 0, 2.5, 5.0, 7.5, and 10 min.

The treated arrays were then covered by a 20 nm-thick gold film, which was sufficient for strong absorption [37]. The morphologies of the resulting plasmonic arrays are shown as SEM images in Fig. 2.

The geometrical distortion of the hexagonal arrays treated by the oxygen plasma can be observed in top-view and cross-section micrographs. Figure 2a, b shows the top-view and cross-section images of the polystyrene array coated by gold for 30 s normal to the array. This shows the initial spherical

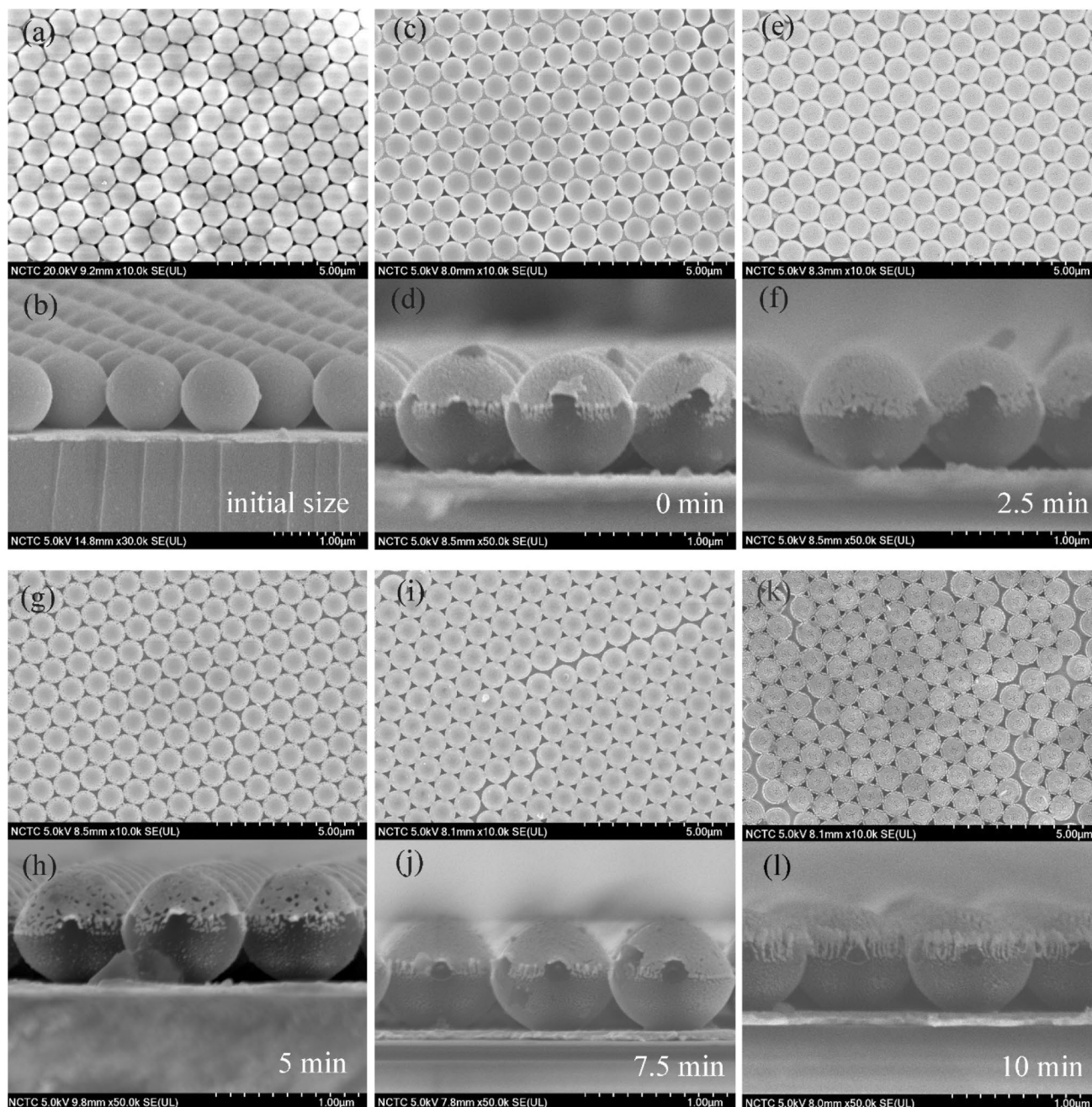


**Fig. 2** Scanning electron micrographs of the top-view and cross-section for (a, b) untreated polystyrene microsphere array, (c, d) untreated polystyrene array with gold sputtering, (e, f) plasma treatment for 2.5 min, (g, h) 5.0 min, (i, j) 7.5 min, and (k, l) 10 min

shape of the polystyrene particles. The plasmonic array was also coated by gold sputtering for 5.0 min, as seen in Fig. 2c, d. These represent the non-plasma-treatment condition.

Comparing the images with gold sputtering for 30 s and 5.0 min, a slight shape distortion occurs when the gold sputtering was performed for a longer time.

The effect of the oxygen-plasma treatment on the polystyrene particles is shown in Fig. 2 for plasma treatment periods of 0 min (c, d), 2.5 min (e, f), 5.0 min (g, h), 7.5 min (i, j), and 10 min (k, l). For comparison, the initial size and shape of the polystyrene particles is shown in Fig. 2 (a, b) in top and side views. In the cross-sectional view, the area above the polystyrene particles appears brighter than the bottom half. This suggests that the thickness of the top half of the gold film was greater than the lower half and this was confirmed by EDX colour mapping. In addition, there are bridging points between adjacent particles as seen by small nodes beside the particles. This was possibly due to the heat from the plasma treatment. The top of the polystyrene particles became cone-shaped after longer treatment times [46]. The vertical height of the upper hemisphere of the polystyrene particles was considerably reduced compared with the height of the lower hemisphere, so the particle shapes resembled asymmetric bi-convex lenses in side view. After a treatment time of 10 min, the vertical heights reduced to 49% of the initial height. The surface appeared rougher when the polystyrene particles were plasma treated for longer times, which is attributed to the forming of C–O–C bonds, from cross-linking [47–49].

The variation of the height and diameter of the treated polystyrene particles as a function of the treatment time is measured and plotted in Fig. 3. The height of the polystyrene particles rapidly reduced from  $885 \pm 13$  nm to  $810 \pm 18$  nm. For treatment times longer than 2.5 min, the height reduced more slowly to  $770 \pm 21$ ,  $740 \pm 14$ , and  $730 \pm 19$  nm, for 5.0, 7.5, and 10 min plasma treatment, respectively. The variation of the height (in nanometers) was fitted to a quadratic function as  $1.49t^2 - 31.3t + 884$  ( $R^2=0.99$ ), where  $t$  is treatment time in min. This trend was valid for the treatment range of 0 to ~10 min. There was a slight change in shape during plasma treatment as the particles became flatter in the top half.

The diameters of the polystyrene microparticles with and without treatment were measured along two axes at  $30^\circ$  to each other within the plane of the array. The first axis, denoted by  $L_1$ , is defined along the direction joining the connecting points between the nearest-neighbor particles and the second axis,  $L_2$ , is defined by the half angle between the connecting axes, i.e.,  $30^\circ$  from  $L_1$ , as illustrated in Fig. 1a. The change in diameter as a function of plasma treatment time is shown in Fig. 3. For treatment times between 0 and 2.5 min, the diameters in  $L_1$  and  $L_2$  are slightly increased. This is attributed to a slight softening of the polystyrene due

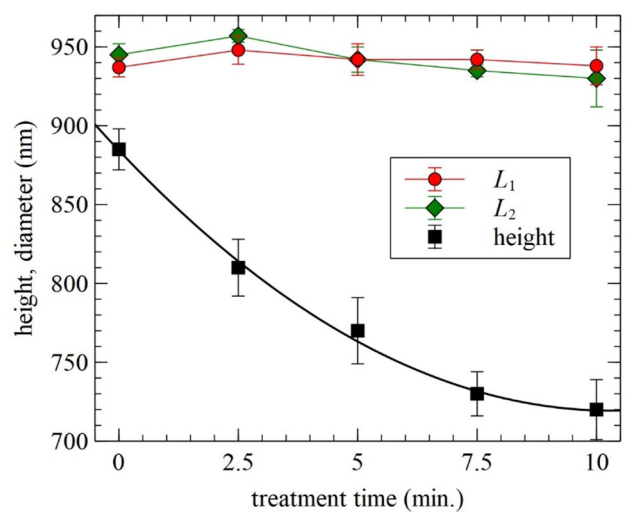


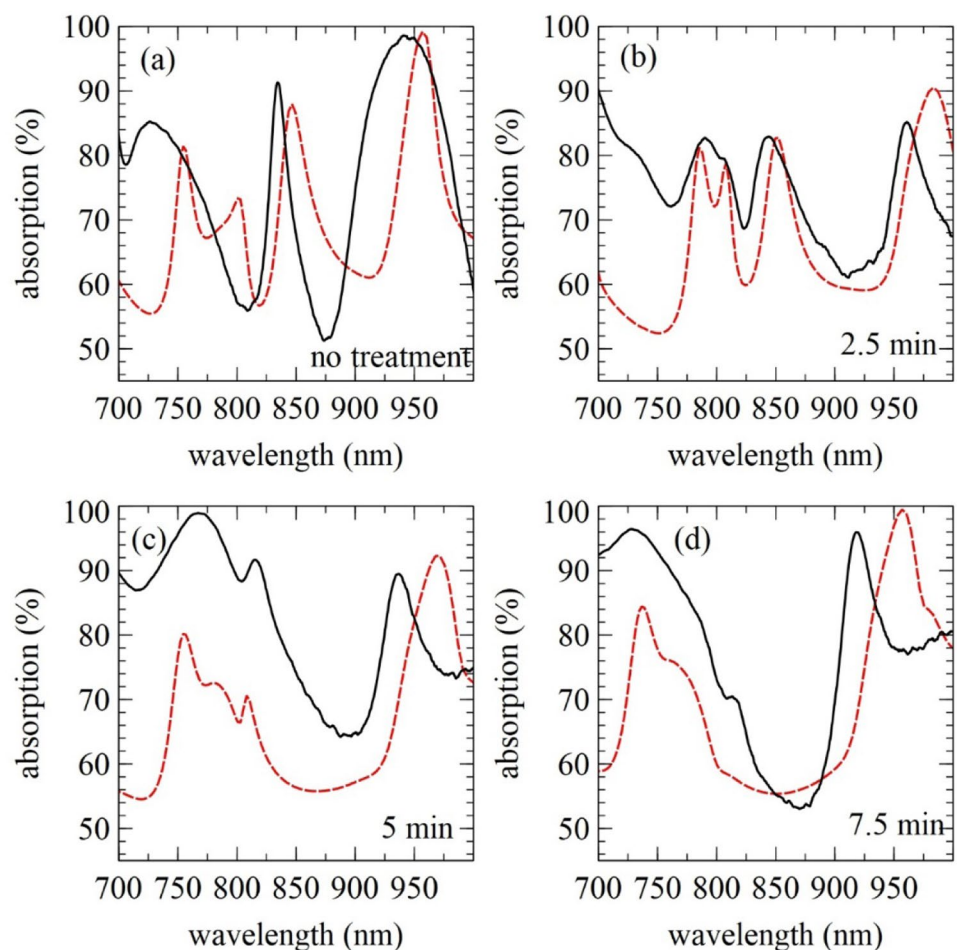
**Fig. 3** Measured geometrical parameters of polystyrene particles treated by oxygen plasma from 0 to 10 min including height (squares), diameter along  $L_1$  axis (red circles) and diameter along  $L_2$  axis (green diamonds)

to heating. However, after 2.5 min, the diameters along the two axes slightly decreased. The final diameter of the polystyrene particle along the  $L_1$  direction after 10 min of plasma treatment was  $938 \pm 12$  nm. The diameter along the second axis decreased to  $930 \pm 18$  nm after 10 min. The diameters measured in the two directions were similar for this plasma treatment cases. However, different rates of chemical reaction of the oxygen plasma on  $L_1$  and  $L_2$  in polystyrene particles have been observed [52], and the changes of  $L_1$  and  $L_2$  due to plasma treatment for 10 min were found to be 0.10% and 1.6%, respectively.

### 3.2 Optical response of gold-capped polystyrene particles compared with FDTD simulations

Optical absorption spectra were determined from the reflection and transmission spectra normal to the film. The measured absorption spectra (black solid lines) were compared to those from the FDTD simulations (red dashed lines) shown in Fig. 4, illustrating (a) no plasma treatment and (b), (c), (d) for oxygen-plasma treatments of 2.5, 5.0, and 7.5 min, respectively. Variations of absorbance spectra measured in different areas and samples are shown in the Supplementary Information. There are three dominant absorption peaks for the untreated array, namely, at 944, 835, and 726 nm. Randomness and defects in the periodicity of the experimental arrays [37] and imperfections in the gold deposition layers may broaden the resonance peaks in the optical spectra. The SEM images showed random voids in the gold near the rim of the semi-shells. This roughened gold surface would reduce reflectivity, again resulting in spectral broadening.

**Fig. 4** Measured optical absorption spectra (solid lines) of the plasmonic hexagonal array treated by oxygen plasma at (a) 0, (b) 2.5, (c) 5.0, and (d) 7.5 min compared with simulated (dashed line) spectra. FDTD simulations computed with (a)  $n=1.58$ ,  $h=860$  nm, (b)  $n=1.70$ ,  $h=795$  nm, (c)  $n=1.70$ ,  $h=720$  nm, and (d)  $n=1.70$ ,  $h=685$  nm



During the gold sputtering process, aggregates of gold particles are deposited onto the substrate. Our simulations suggested that the gold particle aggregates had a negligible effect on the optical resonances when they were far away from the polystyrene particle centre. However, gold particle aggregates close to the polystyrene particles slightly perturbed the optical resonance inside the polystyrene particle, further illustrated in the Supplementary Information.

It is evident from Fig. 4 that the measured and simulated results are consistent for the untreated array, assuming the height of the polystyrene particles as 860 nm and refractive index of 1.58. The simulated height was assumed to be 20 nm less than the SEM observed height to account for the gold film thickness. However, there was an extra peak at a wavelength of 802 nm in the simulation compared to the measurement. In the measured absorption spectrum in Fig. 4(a, black solid line), there is an asymmetric peak in the range of 700–800 nm. This asymmetric peak is possibly a combination of the 802 nm and 755 nm peaks seen in the simulation. Additionally, the missing extra peak in the

measured spectra could be attributed to imperfect packing of the fabricated array. In the simulations, the intensity of the extra peak was more dependent on the packing distance than the other peaks.

The measured absorption spectrum of the plasmonic hexagonal array treated with oxygen plasma at 2.5 min is shown in Fig. 4b (black solid line). In the FDTD simulations with a refractive index of 1.58, to match the spectra, the polystyrene particle height should be  $\sim 850$  nm which is greater than the height estimated from the SEM images. Thus, we chose a smaller polystyrene particle height in the simulations, but also increased the effective refractive index of the polystyrene particles. Previous reports [49, 50] of plasma treatment of a polystyrene film with a thickness of 100 nm yielded a refractive index of up to 2.1 at dense ion fluxes. While this is likely to be a surface modification, we have chosen to model the overall film with an effective refractive index for simplicity. To match the measured and computed spectra to the measured particle height of 795 nm (from SEM images), we approximated

the effective refractive index of the polystyrene as 1.70. However, in the real case, core-shell particles with greater surface refractive index are more likely. As explained in the Supplementary Information Fig. S7, with this simulation, the three models exhibited fairly similar absorption spectra. As the refractive index of the shell increases, the shell would be assumed to be thinner. Resonance modes were shifted to longer wavelength when the refractive index increased. After longer plasma treatments, the absorption peaks decreased in wavelength due to squeezed cavity size, but the individual optical resonance modes responded differently to the geometrical perturbation. For example, the absorption peak at 961 nm treated at 2.5 min decreased by 2.6% after 5.0 min treatment, while the peak to shorter wavelength was shifted by 3.2%. The plasma treatment of the polystyrene particles leads to a geometric distortion. The vertical profile of the particles becomes asymmetric

between the upper and lower hemispheres due to the higher plasma load above. With the vertical asymmetry, the resonances moved to longer wavelengths. However, the resonance wavelengths below 900 nm were less affected by these asymmetries.

The plots of time-averaged electric fields in x-polarization are illustrated in Fig. 5a–f. The fields show a higher number of lobes for higher order resonances. The electric fields were mostly localized inside the polystyrene particle and rarely penetrated into the substrate. The resonance modes are localized between the gold layers and are affected by the periodicity. This can be demonstrated by the different absorption spectra of the plasmonic hexagonal and square packed arrays even with the same polystyrene particle height, as further discussed in the Supplementary Information Fig. 3.

The x-polarized electric field amplitude,  $|E_x|$ , of the untreated array was simulated, and its time average in the

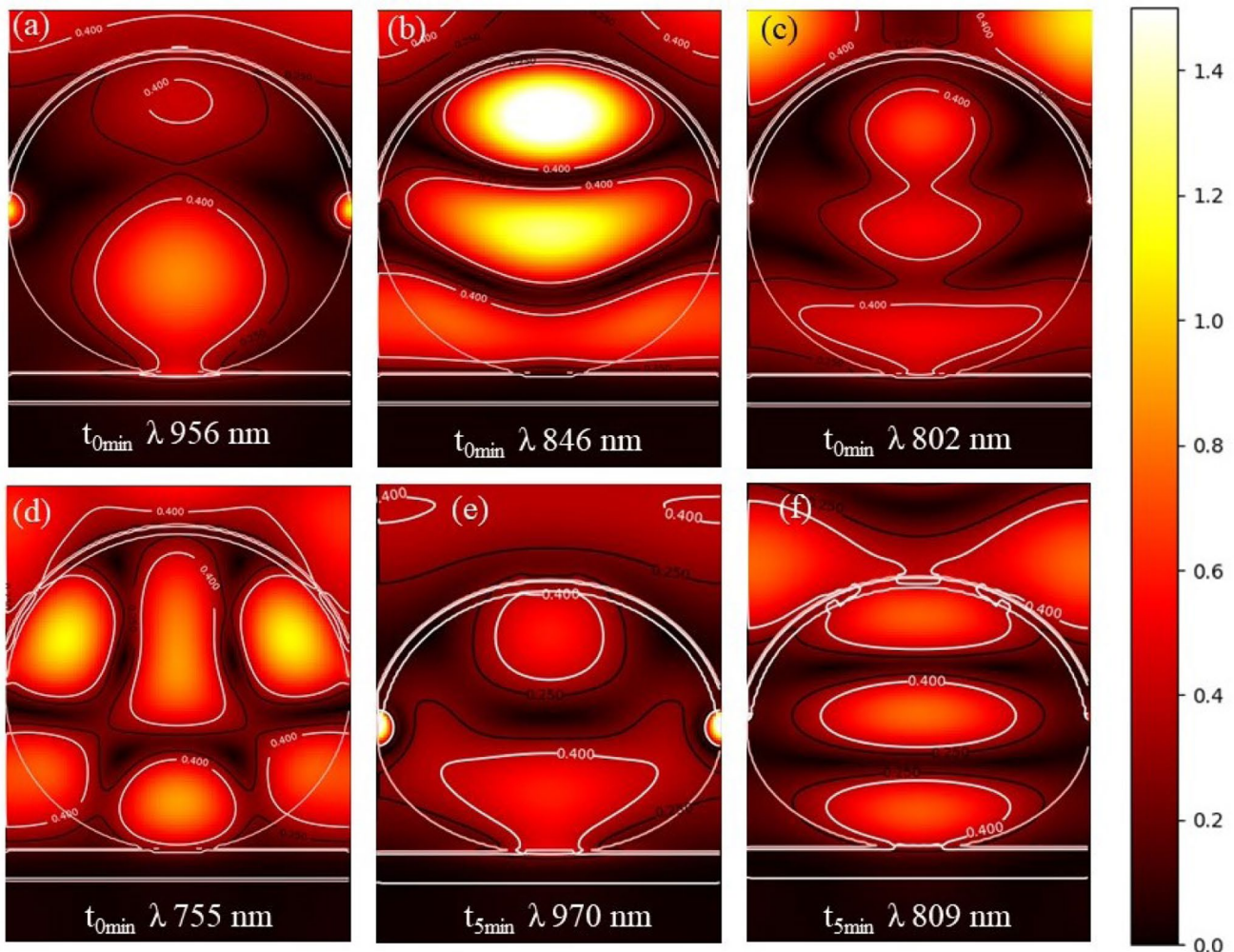


**Fig. 5** FDTD simulations of the polystyrene particle array on a 80 nm-gold substrate capped with 20 nm-gold film calculated with hexagonal boundary condition, and showing the time-averaged elec-

tric field in x-polarization in yz-plane for wavelength of (a) 956, (b) 846, (c) 802, and (d) 755 nm for no plasma treatment case, and (e) 970 and (f) 809 nm for 5 min treatment case

$yz$ -plane is illustrated in Fig. 5a–d, where the field patterns with the strongest electric fields are shown in bright yellow and the weakest fields in dark black. The average electric field for the 956 nm mode had a large lobe at the bottom and a smaller lobe on top of the polystyrene particles. Extra nodes appeared for shorter wavelengths. The average electric field density inside the polystyrene particles was integrated to estimate the optical confinement density. The computed average electric field densities with different substrate refractive indices are shown in Fig. 6a. The untreated polystyrene particles (860 nm height) on a gold substrate confined the electric field at 965 nm wavelength with 1.8 times stronger confinement than that for a dielectric substrate. The electric field density increased as the height of the polystyrene particles was reduced.

To compare alternative photonic and plasmonic structures, the quality factor ( $Q$  factor) of the fabricated plasmonic arrays was computed from the ratio of the central resonance wavelength to its linewidth [30]. These estimated  $Q$  factors of the plasmonic hexagonal array likely arise from extended (propagating) modes of the array. After the oxygen-plasma treatment of duration 0, 2.5, 5.0, and 7.5 min, the  $Q$  factors for the resonance wavelengths in the range of 900 nm to 1000 nm were 11, 26, 24, and 15, respectively. The  $Q$  factors of the plasmonic hexagonal array increased after initial plasma treatment, but decreased for longer treatment times. This initial increase is attributed to the increased uniformity of the gold semi-shell coating layer, because the gold capping layer on the polystyrene particles influences the bandwidth, from the simulations. The upper hemisphere of the polystyrene particles became flatter after plasma treatment, consistent

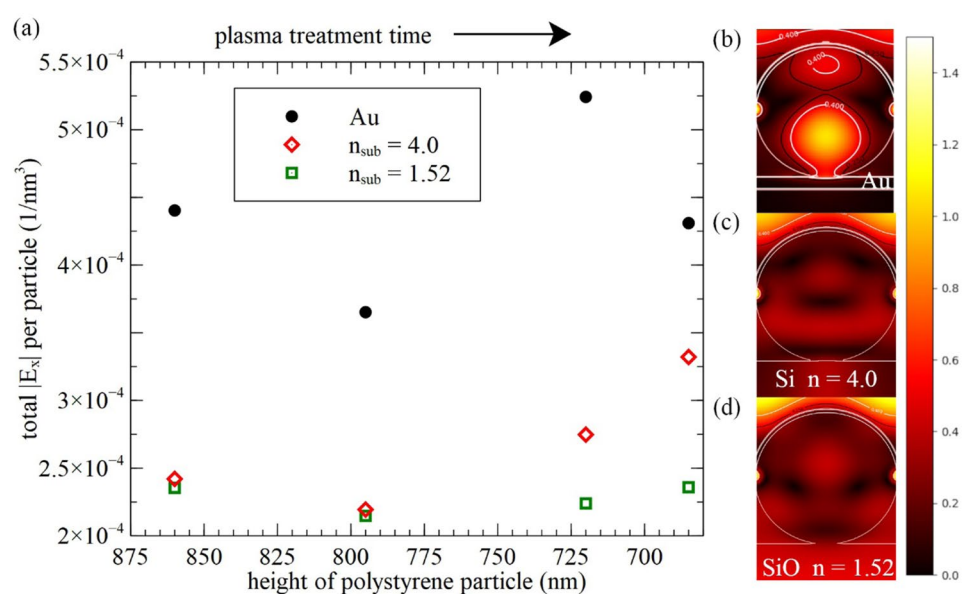
with Refs. [46, 50]. On the other hand, at a wavelength of 836 nm, the non-treated array had a  $Q$  factor of 42, which was comparable to that of a free-standing monolayer of polystyrene ( $Q$  factor of 48) [38]. However, a monolayer array on a gold substrate capped with  $\text{Al}_2\text{O}_3$  had a higher  $Q$  factor of 132 [30].

The resonance modes of the array were modified by oxygen-plasma treatment for different durations. There was competition between optical confinement within the plasma-treated polystyrene particles and energy leakage into the substrate. The plasma treatment increased the refractive index of the polystyrene and spread the gold capping layer more uniformly, increasing the quality factors in the micro-cavities for each resonance mode.

## 4 Conclusions

Hexagonal plasmonic–photonic arrays of polystyrene particles with a range of resonance wavelengths were fabricated by convective deposition, a technique of self-assembly, with a gold substrate and gold capping. The fabricated plasmonic hexagonal array enables concentration of the optical intensity inside the polystyrene particles with strong resonances corresponding to propagating modes. The measured optical spectra were consistent with numerical simulations. The increased optical confinement and strong, tunable resonances of these plasmonic hexagonal arrays show their promise for applications including sensing or enhanced light emission from doped polystyrene gain materials.

**Fig. 6** **a** Total resonant electric field amplitude  $|E_x|$  per particle volume calculated inside the polystyrene particle for various heights and for different substrate refractive index including gold (circle),  $n=4.0$  (red diamond) and  $n=1.52$  (green square), and calculated resonant electric field distribution at about 956 nm in  $yz$ -plane for **(b)** gold, **(c)** silicon ( $n=4.0$ ), and **(d)** glass ( $n=1.52$ )





**Supplementary Information** The online version contains supplementary material available at <https://doi.org/10.1007/s00340-021-07616-7>.

**Acknowledgements** The first author thanks the Thailand Development and Promotion of Science and Technology Talent Program for a scholarship. Research funding under the Research Nanotechnology Network (RNN) of National Nanotechnology Center and from Macquarie University is gratefully acknowledged. This work was supported by the Thailand National Science and Technology Development Agency (P1752706).

## References

- G. Groenhof, J.J. Toppari, *J. Phys. Chem. Lett.* **9**, 4848–4851 (2018)
- A. Bisht, J. Cadra, M. Wersall, A. Canales, T.J. Antosiewicz, T. Shegai, *Nano. Lett.* **19**, 189–196 (2019)
- C. Schneider, P. Gold, S. Reitzenstein, S. Hofling, M. Kamp, *Appl. Phys. B* **122**, 19 (2016)
- L.-W. Nien, K. Chen, Th. D. Dao, S. Ishii, Ch.-Hw. Hsueh, T. Nagao, *Nanoscale* **9**, 16950 (2017)
- J.D. Caldwell, O.J. Glembocki, Y. Francescato, N. Sharac, V. Giannini, F.J. Bezares, J.P. Long, J.C. Owrutsky, I. Vurgaftman, J.G. Tischler, V.D. Wheller, N.D. Bassim, L.M. Shirey, R. Kasica, S.A. Maier, *Nano Lett.* **13**, 3690–3697 (2013)
- Z.Y. Wang, R.J. Zhang, S.Y. Wang, M. Lu, X. Chen, Y.X. Zheng, L.Y. Chen, Z. Ye, C.Z. Wang, K.M. Ho, *Sci. Rep.* **5**, 7810 (2015)
- D. Visser, S.B. Basuvalingam, Y. Desieres, S. Anand, *Opt. Express* **27**, 5353–5367 (2019)
- G. Zhang, C. Lan, R. Gao, J. Zhou, *J. Phys. Chem. C* **123**, 28887–28892 (2019)
- Z. Zhang, J. Zhou, Y. Wu, Z. Xia, X. Qin, *Appl. Phys. Lett.* **116**, 113903 (2020)
- S. Yuan, X. Qiu, C. Cui, L. Zhu, Y. Wang, Y. Li, J. Song, Q. Huang, J. Xia, *ACS Nano* **11**, 10704–10711 (2017)
- S.-P. Yu, J.A. Muniz, C.-L. Hung, H.J. Kimble, *PNAS* **116**, 12743–12751 (2019)
- S. Campione, S. Liu, L.I. Basilio, L.K. Warne, W.L. Langston, T.S. Luk, J.R. Wendt, J.L. Reno, G.A. Keeler, I. Brener, M.B. Sinclair, *ACS Photonics* **3**, 2362–2367 (2016)
- L. Shi, X. Liu, H. Yin, J. Zi, *Phys. Lett. A* **374**, 1059–1062 (2010)
- S. Cushing, L.A. Hornak, J. Lankford, Y. Liu, N. Wu, *Appl. Phys. A* **103**, 955–958 (2011)
- Y. Li, J. Sun, L. Wang, P. Zhan, Zh. Cao, Zh. Wang, *Appl. Phys. A* **92**, 291–294 (2008)
- T. Endo, K. Kerman, N. Nagatani, H.M. Hiepa, D.-K. Kim, Y. Yonezawa, K. Nakano, E. Tamiya, *Anal. Chem.* **78**, 6465–6475 (2006)
- X. Hou, Q. Wang, G. Mao, H. Liu, R. Yu, X. Ren, *Appl. Surf. Sci.* **437**, 92–97 (2018)
- Z. Yi, G. Niu, J. Luo, X. Kang, W. Yao, W. Zhang, Y. Yi, Y. Yi, X. Ye, T. Duan, Y. Tang, *Sci. Rep.* **6**, 32314 (2016)
- J. Lee, Q. Zhang, S. Park, A. Choe, Zh. Fan, H. Ko, A.C.S. *Appl. Mater. Interfaces* **8**, 634–642 (2016)
- Z. Cai, Z. Xiong, X. Lu, J. Teng, *J. Mater. Chem. A* **2**, 545–553 (2014)
- B. Ding, M. Bardosova, M.E. Pemble, A.V. Korovin, U. Peschel, S.G. Romanov, *Adv. Funct. Mater.* **21**, 4182–4192 (2011)
- L. Wu, G. Kim, H. Nishi, T. Tatsuma, *Langmuir* **33**, 8976–8981 (2017)
- K. Sugawa, T. Tamura, H. Tahare, D. Tamaguchi, T. Akiyama, J. Otsuki, Y. Kusaka, N. Fukuda, H. Ushijima, *ACS Nano* **7**, 9997–10010 (2013)
- J.R. Lacowicz, C.D. Geddes, I. Gryczynski, J. Malicka, Z. Gryczynski, K. Aslan, J. Lukomska, E. Matveeva, J. Zhang, R. Badugu, J. Huang, *J. Fluoresc.* **14**, 425–441 (2004)
- M. López-García, J. Galisteo-López, A. Blanco, J. Sánchez-Marcos, C. López, A. García-Martín, *Small* **6**, 1757–1761 (2010)
- Y. Yang, G.P. Wang, *Appl. Phys. Lett.* **89**, 111104 (2006)
- Z. Liu, G. Liu, X. Liu, S. Huang, Y. Wang, P. Pan, M. Lie, *Mater. Lett.* **158**, 262–265 (2015)
- L. Tang, B. Wu, P. Tang, M. Liu, X. Zhan, X. Liu, Z. Liu, *Opt. Mater.* **91**, 58–61 (2019)
- A.M.M. Gherman, A. Vladescu, A.E. Kiss, C. Farcau, *Photonics Nanostructures: Fundam. Appl.* **38**, 100762 (2020)
- B.X. Yu, L. Shi, D. Han, J. Zi, P.V. Braun, *Adv. Funct. Mater.* **20**, 1910–1916 (2010)
- Zh. Liu, M. Yu, Sh. Huang, X. Liu, Y. Wang, M. Liu, P. Pan, G. Liu, *J. Mater. Chem. C* **3**, 4222–4226 (2015)
- C. Farcau, M. Giloan, E. Vinteler, S. Astilean, *Appl. Phys. B* **106**, 849–856 (2012)
- C.A. Tira, I. Ly, R.A.L. Vallee, S. Astilean, C. Farcau, *Opt. Mater. Express* **7**, 2847–2859 (2017)
- C. Farcau, *Sci. Rep.* **9**, 3683 (2019)
- R. Cole, Y. Sugawara, J. Baumberg, S. Mahajan, M. Abdelsalam, P. Bartlett, *Phys. Rev. Lett.* **97**, 137401 (2006)
- M. Lopez-Garcia, J.F. Galisteo-Lopez, C. Lopez, A. Garcia-Martin, *Phys. Rev. B* **85**, 235145 (2012)
- Z. Liu, L. Liu, H. Lu, P. Zhan, W. Du, M. Wan, Z. Wang, *Sci. Rep.* **7**, 43803 (2017)
- P. Gu, L. Qian, Z. Yan, W. Wu, Z. Chen, Z. Wang, *Opt. Commun.* **419**, 103–107 (2018)
- F. Di Stasio, L. Berti, S.O. McDonnell, V. Robbiano, H.L. Anderson, D. Comoretto, F. Cacialli, *APL Mater.* **1**, 042116 (2013)
- D. Rout, R. Vijaya, *J. Appl. Phys.* **119**, 023108 (2016)
- L. Shi, M. Zheng, F. Jin, X. Dong, W. Chen, Z. Zhao, X. Duan, *Appl. Opt.* **55**, 4759–4762 (2016)
- J. Feng, Sh. Bian, Y. Long, H. Yuan, Q. Liao, H. Cai, H. Huang, K. Song, G. Yang, *J. Mater. Chem. C* **1**, 6157–6162 (2013)
- N. Vogel, S. Goerres, K. Landfester, C.K. Weiss, *Macromol. Chem. Phys.* **212**, 1719–1734 (2011)
- C. Stelling, C. Bernhardt, M. Retsch, *Macromol. Chem. Phys.* **216**, 1682–1688 (2015)
- X. Song, Z. Dai, X. Xiao, W. Li, X. Zheng, X. Shang, X. Zhang, G. Cai, W. Wu, F. Meng, C. Jiang, *Sci. Rep.* **5**, 17529 (2015)
- B.J. Tan, C. Sow, K. Lim, F. Cheong, G. Chong, A. Wee, C. Ong, *J. Phys. Chem. B* **108**, 18575–18579 (2004)
- Z.A. Lewicka, A. Bahloul, W.W. Yu, V.L. Colvin, *Nanoscale* **5**, 11071–11078 (2013)
- E. Kosobrodova, A. Kondyurin, D.R. McKenzie, M.M.M. Bilek, *Nucl. Instr. Methods. Phys. Res. B* **304**, 57–66 (2013)
- S. Ye, H. Wang, H. Su, L. Chang, S. Wang, X. Zhang, J. Zhang, B. Yang, *J. Mater. Chem. C* **5**, 3962–3972 (2017)
- S. Soleimani-Amiri, A. Gholizadeh, S. Rajabali, Z. Sanaee, S. Mohajerzadeh, *RSC Adv.* **4**, 12701–12709 (2014)
- E.M. Akinoglu, A.J. Morfa, M. Giersig, *Langmuir* **30**, 12354–12361 (2014)
- F.J. Wendisch, R. Oberreiter, M. Salihovic, M.S. Elsaesser, G.R. Bourret, *A.C.S. Appl. Mater. Interfaces* **9**, 3931–3939 (2017)
- L. Luo, E.M. Akinoglu, L. Wu, T. Dodge, X. Wang, G. Zhou, M.J. Naughton, K. Kempa, M. Giersig, *Nanotechnology* **31**, 245302 (2020)
- B.K. Gan, A. Kondyurin, M.M.M. Bilek, *Langmuir* **23**, 2741–2746 (2007)

55. A. Kondyurin, B.K. Gan, M.M.M. Bilek, D.R. McKenzie, K. Mizuno, R. Wuhler, Nucl. Instr. Methods. Phys. Res. B **266**, 1074–1084 (2008)
56. B. K. Gan., M. M. M. Bilek, A. Kondyurin, K. Mizuno, D. R. McKenzie, Nucl. Instr. Methods. Phys. Res. B **247**, 254–260 (2006)
57. Y. Han, X. Huang, A.C.W. Rohrbach, C.B. Roth, J. Chem. Phys. **153**, 044902 (2020)
58. M.M.M. Bilek, A. Kondyurin, S. Dekker, B.C. Steel, R.A. Wilhelm, R. Heller, D.R. McKenzie, A.S. Weiss, M. James, W. Moller, J. Phys. Chem. C **119**, 16793–16803 (2015)
59. T. Muangnapoh, A.L. Weldon, J.F. Gilchrist, Appl. Phys. Lett. **103**, 181603 (2013)
60. M. Joy, T. Muangnapoh, M.A. Snyder, J.F. Gilchrist, Soft Matter **11**, 7092 (2015)
61. A.F. Oskooi, D. Roundy, M. Ibanescu, P. Bermel, J.D. Joannopoulos, S.G. Johnson, Comput. Phys. Commun. **181**, 687–702 (2010)
62. A.D. Rakic, A.B. Djurusic, J.M. Elazar, M.L. Majewski, Appl. Opt. **37**, 5271–5283 (1998)
63. N. Sultanova, S. Kasarova, I. Nikolov, Acta Phys. Pol. A **116**, 585–587 (2009)
64. J.F. Shackelford, *Introduction to Materials Science for Engineers*, 5th edn. (McGraw-Hill, New York, 2000).

**Publisher's Note** Springer Nature remains neutral with regard to jurisdictional claims in published maps and institutional affiliations.